Sources of backscatter at 5.3 GHz from a superimposed ice and firn area revealed by multi-frequency GPR and cores

Kirsty LANGLEY,[1*] Pascal LACROIX,[2] Svein-Erik HAMRAN,[1] Ola BRANDT[3†]

[1]*University of Oslo, PO Box 1042, Blindern, NO-0316 Oslo, Norway*
E-mail: Kirsty.langley@polar.no
[2]*Legos, 14 av. Edouard Belin, 31400 Toulouse Cedex, France*
[3]*Norwegian Polar Institute, Polar Environmental Centre, NO-9296 Tromsø, Norway*

ABSTRACT. We investigate the major sources of backscatter at 5.3 GHz, within the superimposed ice and firn areas of a polythermal glacier. Two ground-penetrating radar systems, an 800 MHz impulse system and a polarimetric 5.3 GHz frequency-modulated continuous-wave system, are used to acquire along-glacier profiles in the accumulation area of Kongsvegen, Svalbard. The 800 MHz response is used to map reflection horizons in the glacier. Using cores from the superimposed ice and firn areas, the causes of these reflection horizons, in terms of snow, firn and ice layers, are investigated. Superimposing the reflection horizons on the co-polarized and cross-polarized 5.3 GHz profile, we are able to determine how the 5.3 GHz frequency responds to the different media. Scattering at rough interfaces and volume scattering occur in the superimposed ice area and are apparently caused by air-bubble number, size and distribution. In the firn the strongest return originates from below the previous summer surface, consistent with previous findings. At approximately the same depth, strong incoherent scattering begins. The rapid decrease in coherent reflections indicates the significance of scattering in the firn.

INTRODUCTION

Monitoring of the world's glaciers to assess any climate signature they may provide is a key concern in the field of glaciology. This effort is greatly aided by the use of satellite remote sensors, and in particular by those operating in the microwave frequency range (Bamber and Kwok, 2004). Using such frequencies, the resulting images show not only surface reflectivity but also backscatter from properties at depth. This leads to uncertainty as to where, within the depth profile, the main contribution to the backscatter signal originates.

Penetration and scattering of the electromagnetic (EM) waves is an important factor for satellite-borne synthetic aperture radars (SARs) and altimeters (e.g. Envisat, RADARSAT, the Advanced Land Observing Satellite (ALOS) and the planned CryoSat-2). Returns from the subsurface can, for example, cause digital elevation model errors (Berthier and others, 2006), loss of coherence in the interferometric process (Rignot and others, 2001) and biasing of altimeter measurements (Helm and others, 2007). The induced height difference differs from Ku- to S-bands (Legrésy and others, 2005) due to the difference in radar sensitivity to the snow scattering properties (Lacroix and others, 2007). Studies to assess this subsurface effect are important for proper interpretation of satellite data. Ground-penetrating radar (GPR) is a common tool for glaciological investigations (Daniels, 2004). Whilst side-looking satellite SAR instruments give two-dimensional images with a single backscatter value per pixel (which is the sum of all contributions to the depth of penetration), the GPR time window is subdivided to give backscatter at different depths. GPR instruments are commonly operated in single polarization mode, although interest in polarization effects has increased as polarimetric capabilities become a more common feature of satellite SARs (Stebler and others, 2005). We are concerned with linear polarization where the orientation of the electric field component of the EM wave is forced by the transmit and receive antennas to be either the same (co-polarized) or perpendicular (cross-polarized).

It is instructive to consider how the response of the two polarizations will differ. A strong co-polarized response will occur at a flat dielectric interface. The greater the dielectric contrast, the greater the backscatter. Once the surface is no longer flat with respect to the radar wavelength, scattering will occur at the interface, with possible depolarization of the wave. This will reduce the proportion of energy backscattered in the co-polarized plane and increase it in the cross-polarized plane. Hence we can expect a co-polarized response from both a smooth and a rough interface, although for the former the peak amplitude will be greater and width of the response narrower. A cross-polarized response will only occur when depolarized scattering is involved. This requires either a rough dielectric interface, or scattering from inhomogeneities within a volume. The magnitude of the polarized responses is linked since the incident energy is finite and is the input to both responses. The cross-polarized backscatter response is less than the co-polarized response. The exception to this is when the illuminated medium is such that all incoming energy is scattered homogeneously in all directions, in which case the co- and cross-polarized responses will be equal. Ulaby and others (1981) provide a more in-depth discussion on polarization and scattering. The use of ground-based radars (Jezek and others, 1994; Scott and others, 2006a; Langley and others, 2007) and airborne systems (Hawley and others, 2006; Helm and others, 2007) allows the investigation of scattering with depth, an aspect integrated into the satellite response.

*Present addresses: Norwegian Polar Institute, Polar Environmental Centre, NO-9296 Tromsø, Norway; Institute of Physics and Technology, University of Tromsø, NO-9037 Tromsø, Norway.
†Present address: Norwegian Mapping Authority, Fylkeshuset, Todenskjoldsgate 65, NO-4614 Kristiansand, Norway.

https://doi.org/10.3189/002214309788608660 Published online by Cambridge University Press

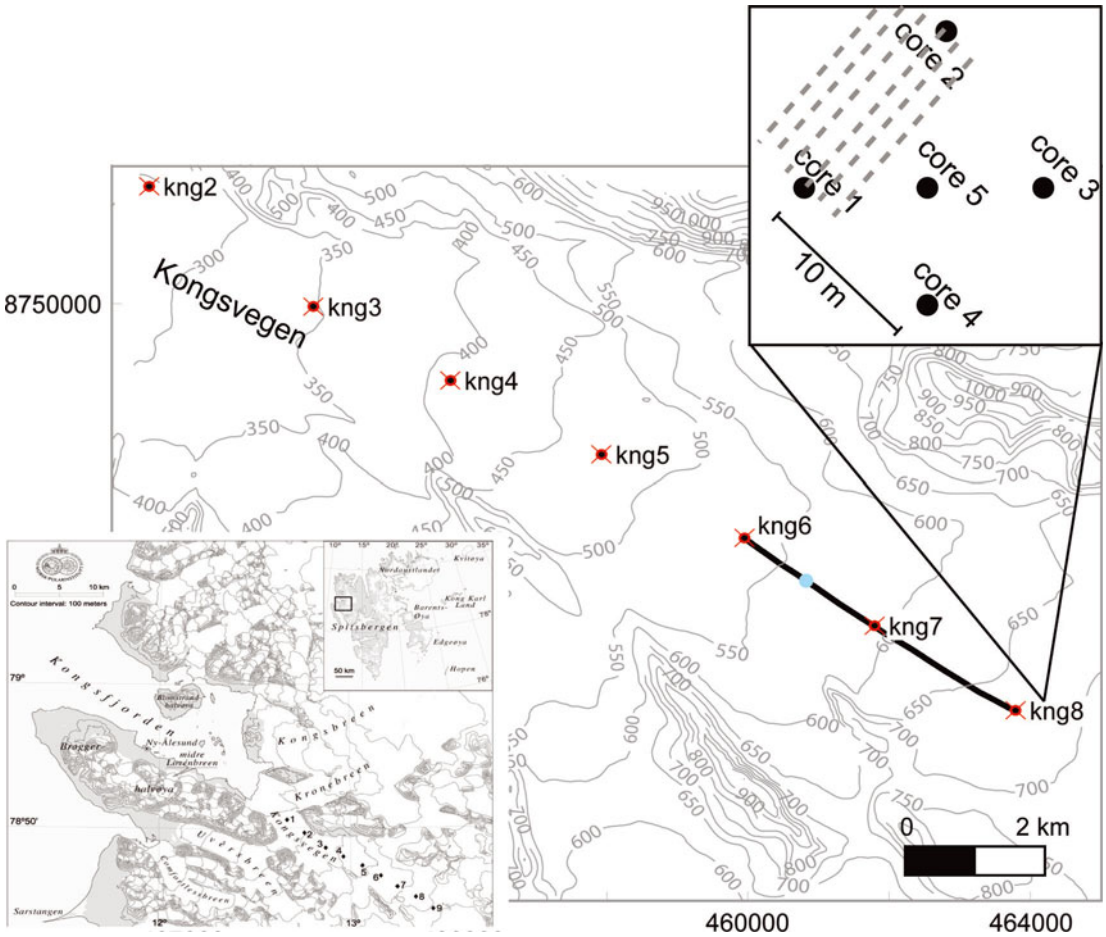

Fig. 1. Lower left inset: location of Kongsvegen in Svalbard. Main panel: upper section of Kongsvegen. The red crosses mark the mass-balance stakes along the centre line of the glacier. An along-glacier radar profile was measured between stakes 6 and 8, indicated by the black curve. The blue dot shows the location of a superimposed ice core. Upper inset: The location of firn cores at stake 8, along with a schematic of radar lines measured within the grid (grey dashed lines).

Recent work in Greenland targets the percolation facies. This is considered to be an important zone for the storage of water (Bøggild and others, 2005). For the higher-frequency altimeter system, it has been shown that during spring the previous summer surface (PSS) at the base of the winter snowpack gives the strongest return (Scott and others, 2006b; Helm and others, 2007). Higher-density features within the snowpack, such as wind crusts and ice layers, also give a strong backscatter contribution, as do thin ice layers at or just below the PSS. At C-band, similar results were obtained by Jezek and others (1994), although they identify an ice layer zone as being the major backscatter source.

On Svalbard, the accumulation area of glaciers commonly consists of superimposed ice and firn. Superimposed ice is formed when saturated snow and firn facies or ponded meltwater freeze (Paterson, 1994). This constitutes an often unknown, but in some cases significant, component of the annual accumulation (Wadham and Nuttall, 2002). Local topography plays an important role in the formation of the superimposed ice since lower-gradient slopes allow ponding of meltwater (Obleitner and Lehning, 2004) while drainage channels effectively remove the meltwater, limiting superimposed ice formation (Brandt and others, 2008). The time of superimposed ice formation (spring or autumn) influences the number and size of air bubbles trapped in the ice (Wadham and Nuttall, 2002; Obleitner and Lehning, 2004). Variations in the number of bubbles over depth are inferred to be the cause of subsurface radar reflections (König and others, 2002; Wadham and others, 2006). Since melting occurs at all elevations at our study site, the glacier Kongsvegen, the firn area is exposed to meltwater which forms ice layers, lenses, pipes and lower-density depth-hoar layers in the firn and the winter snowpack. Their presence strongly influences the radar response (Jezek and others, 1994; Arcone, 2002; Wadham and others, 2006).

In this study, we investigate the major sources of backscatter at 5.3 GHz, within the superimposed ice and firn areas of a polythermal glacier. To do this we present a qualitative comparison between GPR profiles acquired with a 5.3 GHz polarimetric frequency-modulated continuous-wave (FMCW) radar and an 800 MHz impulse radar respectively. With the impulse system, we identify and map individual reflection horizons. Cores taken in the superimposed ice and firn areas provide a link to the cause of the reflections seen in the radar profile. By superimposing the mapped horizons onto the C-band profile and comparing the location of the greatest backscatter response, we are able to locate the causes of backscatter at 5.3 GHz in terms of the snow, ice and firn properties.

FIELD SITE

Our field site is the 25 km long, polythermal, surge-type glacier, Kongsvegen, situated at ~79° N on the northwest of

https://doi.org/10.3189/002214309788608660 Published online by Cambridge University Press

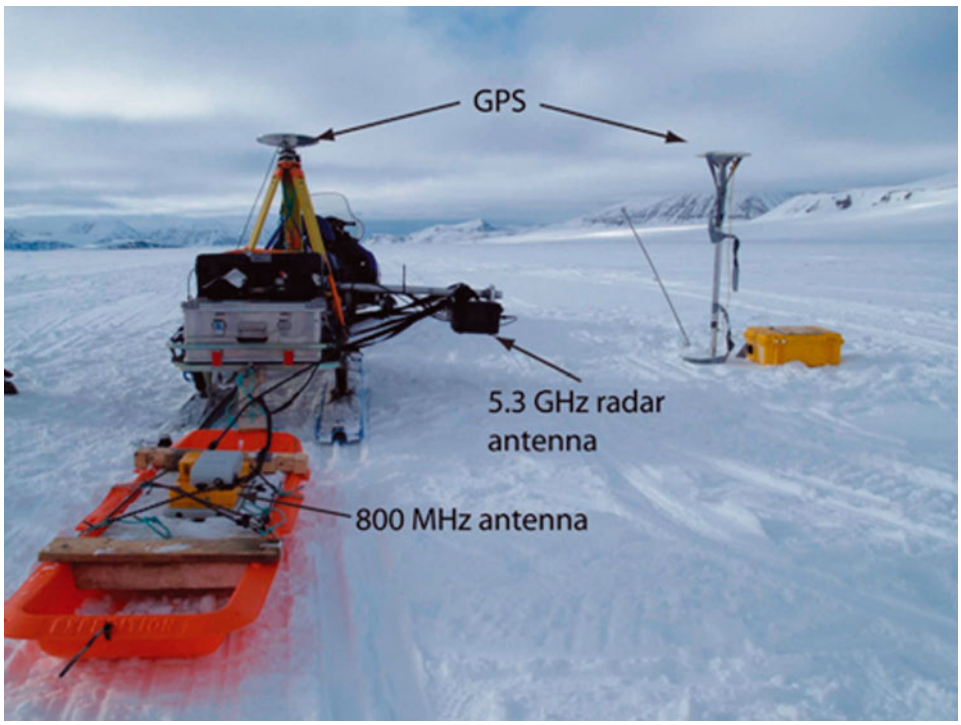

Fig. 2. Field set-up of the radars and GPS. The 5.3 GHz antennas are in the black box protruding to the right of the sledge. The 800 MHz antennas are dragged behind on a plastic sledge.

the Spitsbergen archipelago (Fig. 1) (Liestøl, 1988; Björnsson and others, 1996; Melvold and Hagen, 1998). The glacier has a low surface slope of 0.5–2°. It covers an area of approximately 100 km^2, draining northwestwards from 800 m a.s.l. to sea level. The equilibrium line lies at approximately 500 m a.s.l. (Melvold and Hagen, 1998). The accumulation area is composed of a superimposed ice zone and a firn area at higher altitude. There is no dry-snow zone on Kongsvegen. Melting or rain events can occur year-round in Svalbard, and, during summer, air temperatures typically remain above freezing. Subsequent refreezing of meltwater results in the formation of ice layers, lenses and pipes. These structures can be of various shapes, sizes and orientation, and alter the composition of the snow and firn, resulting in a variable density distribution.

DATA AND PROCESSING

Our field data consist of GPR profiles at 5.3 GHz and 800 MHz, an ice core from the superimposed ice area and five firn cores from the firn area. The fieldwork was carried out during April–May 2005. The air temperature for the duration of the field campaign was below 0°C.

Radar profiles were collected along the centre line of the glacier from the ablation area to the accumulation area, following an existing stake network (Fig. 1). We discuss the 5 km section of the profile from stake 6 in the superimposed ice area to stake 8 in the firn area. The two radars were operated simultaneously from a single snow scooter (Fig. 2). We observed no interference between the instruments. A differential global positioning system (GPS) with a horizontal accuracy of 10 cm was used to locate the profiles. The positions of traces were obtained by matching time stamps in the GPR and GPS.

800 MHz impulse radar

The 800 MHz radar was a Malå Geoscience RAMAC system with 800 MHz shielded antennas (essentially a ground-coupled bowtie). The antennas were placed on a plastic sledge and dragged behind the snow-scooter sledge (Fig. 2). Pulses were triggered at a rate of 4 traces s^{-1}. At our average driving speed of 8 km h^{-1} this corresponds to 2 traces m^{-1}. Each trace was resolved with 1024 samples at 16 bits over a time window of 186 ns so that one wavelength (in air) is resolved by seven samples. Most commercial GPRs are built with a bandwidth approximately equal to the centre frequency; the resolution of the radar is therefore approximately 19 cm in air or 10 cm in ice (using an average relative permittivity, $\varepsilon_r = 3.15$ for ice). Processing was performed using the software ReflexW (http://www.sandmeier-geo.de) and included a dewow filter (removing low-frequency signals within each trace) and background removal (to remove horizontally constant signals which are mainly instrumental noise). The system noise, calculated as the mean signal level before the direct wave, normalized to the peak direct wave power, is –26 dB.

5.3 GHz frequency-modulated continuous-wave (FMCW) radar

The radar used to acquire the 5.3 GHz data was a polarimetric FMCW radar (Hamran and Langley, 2006). The antennas are dual-ridged horns with a gain of 6.6–7.4 dB and a 3 dB beamwidth of 70–65° in both planes over the bandwidth used. They are contained in a box suspended 30 cm above the snow surface on an arm protruding from the side of the snow-scooter sledge (Fig. 2). The frequency sweep is 4.8–5.8 GHz, giving a centre frequency of 5.3 GHz and a bandwidth of 1 GHz. We acquired 2 traces m^{-1}, although the sweep itself only takes 20 ms.

https://doi.org/10.3189/002214309788608660 Published online by Cambridge University Press

Fig. 3. Top 117 cm of the superimposed ice core, taken 1 km up-glacier from stake 6; 0 cm is at the previous summer surface. The different textures seen are due to varying air-bubble content (air bubbles are dark).

We refer to polarization in terms of *X* and *Y*, whereby the *X* plane is aligned in the direction of the GPR travel (i.e. along glacier) and the *Y* plane is perpendicular to the direction of travel (i.e. across glacier). The data were collected and processed in the frequency domain. A Hamming window was applied to reduce the side lobes, followed by conversion to the time domain with a fast Fourier transform algorithm. The bandwidth of 1 GHz should yield a resolution of 0.15 cm in air (Daniels, 2004). However, a side effect of the Hamming window is a broadening of the main lobe, which influences the obtainable resolution. Inspection of the data suggests that the filter causes a 25% broadening of the main lobe. Resolution is therefore reduced to 1.25 ns, equal to 19 cm in air or 10 cm in ice ($\varepsilon_r = 3.15$).

The data were calibrated using a technique proposed by Sarabandi and others (1990) for field calibration of polarimetric radars. The method determines the phase and amplitude deviations in the antennas from the nominal gain values. These field transfer functions were obtained using two reference targets: a sphere with radar cross-section 0.1 m^2 and a diplane, which has a strong cross-polarized radar cross-section. This method is particularly applicable to field operations, as it does not require accurate alignment of the calibration targets or knowledge of the radar cross-section of the depolarizing target (i.e. the diplane) (Sarabandi and others, 1990). For the calibration measurements, the calibration targets were placed at a horizontal distance of 1 m from the radar. To improve the signal-to-noise ratio, a measurement was also made without the targets, allowing the background signal to be removed.

Comparison of the different polarizations shows that the co-polarized channels *YY* and *XX* are approximately equal, as are the cross-polarized channels *YX* and *XY*. Thus we limit ourselves to the presentation of the *YY* and *YX* data as representation of the co- and cross-polarized responses respectively. There is some noise (system artifacts) in the *X* channel, which is noticeable in the figures as a horizontal banding. The system noise, calculated as the mean signal level after the direct wave for a shot in air, and normalized to the maximum profile value, is –28 dB for the co-polarized channel and –8 dB for the cross-polarized channel.

Radar backscatter using the radar equation

In order to compare the two radar systems we convert the radar response to a scattering cross-section, σ_M, σ_{YY} and σ_{YX} (where the subscript M denotes the 800 MHz frequency, and *YY* and *YX* the co-and cross-polarized channels of the FMCW 5.3 GHz radar). σ_q (where $q = M$, *YY* or *YX*) was calculated according to the standard radar equation (Ulaby and others, 1981),

$$\sigma_q(R) = \frac{P_r R^4 (4\pi)^3}{P_t \lambda^2 G^2 V_s} e^{4\alpha R}, \quad (1)$$

where P_t and P_r are the transmitted and received power, G is the antenna gain, λ is the wavelength, V_s is the scattering volume, R is distance from the radar, and α is attenuation.

Wavelength is dependent on the velocity profile of the medium, as is the scattering volume which also includes ray bending at interfaces. Velocity profiles are based on density measurements in snow pits and common-midpoint (CMP) measurements taken at stakes 6–8. An average velocity of 231 m μs^{-1} is used for the snowpack. For ice and firn, bulk velocities derived from the CMP measurements of 190 m μs^{-1} and 220 m μs^{-1} respectively are used. These are constant over depth.

Radar-specific parameters such as antenna gain and beamwidth (necessary for the calculation of the scattering volume) are unknown for the 800 MHz radar, and arbitrary values were assigned (gain of 7 dB, beamwidth of 60°). This is justified since these parameters are constants and are applied to each trace, resulting in a constant trace offset.

Attenuation, α, is a combination of the absorption and scattering losses experienced by the wave as it travels through the medium. In ice, the absorption is frequency-dependent (Robin and others, 1969). Extrapolating from the graphs provided by Robin and others (1969), loss due to absorption in ice at –1°C is on the order of 0.08 dB m^{-1} at 800 MHz and 0.32 dB m^{-1} at 5.3 GHz. In addition, the loss due to scattering from air bubbles will be greater at 5.3 GHz than at 800 MHz, but is an unknown quantity. In the firn, attenuation is estimated from dielectric profiling of the firn cores (described below). An average conductivity of 7 $\mu s\, m^{-1}$ was measured, giving a loss tangent very much lower than 1 (i.e. $\varepsilon''/\varepsilon' \ll 1$), indicating this to be a very low-loss medium. Absorption losses are therefore assumed to be frequency-independent and much lower than in the ice. According to our assumptions, attenuation in the firn is thus due to scattering losses, which are very much greater at 5.3 GHz than at 800 MHz, but again undetermined. Since the actual attenuation is unknown, this term remains a factor in our calculated scattering cross-section, and the values presented here are weighted scattering cross-sections, σ_{wq}:

$$\sigma_{wq} = \sigma_q e^{-4\alpha R}. \quad (2)$$

From σ_{wq}, the backscatter coefficient σ^0_{wq} is calculated as the sum of all scattering responses over the length of each trace:

$$\sigma^0_{wq} = \int_0^R \sigma_{wq(R)}\, dR. \quad (3)$$

This integration is performed from 0 to the depth equivalent of 100 ns so that the same time window is applied to both radar systems. Changing the integration time window beyond 50 ns does not significantly alter the pattern of backscatter along the radar profiles.

Our use of σ_{wq} and σ^0_{wq} is for a relative comparison of backscatter along the profile as measured by the two radar systems. The focus is therefore on the relative changes rather than the absolute values.

https://doi.org/10.3189/002214309788608660 Published online by Cambridge University Press

Superimposed ice core

A single 5 m long core was taken in the superimposed ice area (location indicated in Fig. 1). Digital images with below and side lighting were taken of the whole core length. The images (9 m^{-1}) were stitched together to form a single image of the core (Sjögren and others, 2007), illustrating the variability and range of structures within the ice (Fig. 3). Due to the lighting, clear ice is white, whereas bubbles show up as black. An attempt was made to weigh representative sections within the core to obtain density estimates, but this was unsuccessful. Instead, to obtain a measure of the variability of the bubble content along the core, we integrate the digital image pixel values across the core. The values are then normalized, smoothed and thresholded at 70% to highlight where the highest and lowest bubble concentrations are.

Firn core

Five firn cores, each approximately 10 m long, were recovered in a 10 m grid in the firn area (Fig. 1). The cores were analysed with a dielectric profiler (DEP) instrument (Wilhelms and others, 1998) and digital imagery for visual interpretation. The digital imagery was done using a similar set-up to that for the superimposed ice core but using side lighting (Sjögren and others, 2007). In this case, firn appears bright and ice dark (Fig. 4). The DEP instrument measures the capacitance, C, and conductance, G, of the ice and firn at 250 kHz in 5 mm steps along the cores. The electrodes are 10 mm long and the measurements are influenced by the material properties over approximately a 30 mm window, so data close to cracks in the ice/firn have been excluded.

The DEP measurements are converted to relative permittivity, ε_r (non-dimensional), and conductivity, cond (S m^{-1}), according to (Kohler and others, 2003):

$$\varepsilon_r = \frac{C}{C_{air}}, \quad \text{cond} = \frac{\varepsilon_{air} G}{C_{air}}, \tag{4}$$

where $\varepsilon_{air} = 8.854187 \times 10^{-12}$ F m^{-1} is the permittivity in vacuum and $C_{air} = 64.5 \times 10^{-15}$ F is the free-air capacitance, a constant obtained by taking a reading with an empty instrumental set-up. Density (in kg m^{-3}) is then calculated from (Kovacs and others, 1995; Eisen and others, 2002):

$$\rho = \frac{\sqrt{\varepsilon_r} - 1}{0.000845}. \tag{5}$$

The density differences within the core (i.e. firn or ice) are much larger than the absolute accuracy of the measurements, thereby justifying the relatively simple conversion made with Equation (5).

Due to the smoothing nature of the sample window (approximately 30 cm), abrupt changes in density, transitions that are not horizontally flat, and very thin layers are probably not correctly resolved. This is problematic for GPR comparisons since the nature of an interface (with respect to the radar wavelength) is important for determining how the wave will be reflected. It is for this reason that we complement the DEP record with digital images.

The winter snowpack at the time of data collection was nearly 2 m deep. Since this snow is less consolidated and thus not suitable for transportation, the actual DEP measurements start at approximately 1.8 m depth, the top of the firn. The permittivity profile of the snowpack was obtained from density measurements in snow pits about 10 m away from the core sites, and by bulk weight/volume measurements of the upper core pieces that were not transportable.

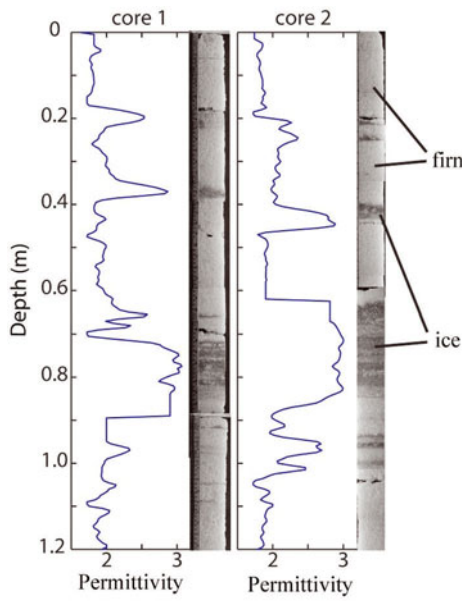

Fig. 4. Digital imagery of the upper sections of firn cores 1 and 2, along with the DEP-derived permittivity profiles. Firn appears white and ice dark. The depth scale starts at the previous year's summer surface.

These processing steps give a density vs depth profile for each core. To compare these profiles with the GPR profiles, the depth scale is converted to two-way travel time, TWT, using:

$$\text{TWT} = \sum_{z=0}^{Z} 2\Delta z \sqrt{\varepsilon_r}/v_{air}, \tag{6}$$

where Δz is the depth interval, Z is the total depth and $v_{air} = 3 \times 10^8$ m s^{-1}. The profiles (examples in Fig. 4) are interpreted visually where high values indicate ice and low values indicate firn.

RESULTS AND DISCUSSION

Figure 5 gives an overview of the radar profiles discussed. For display purposes, the radar profiles (displaying normalized radar cross-section) have been stacked (ten-trace stack). The cross-polarized profile (Fig. 5c) has been normalized to the maximum co-polarized value to allow the difference in backscatter level to be seen. In the profiles we see the winter snowpack, from 0 ns to approximately 15 ns, overlaying the PSS, which is the first continuous interface. The normalized integrated backscatter coefficient σ^0_{wq} is given in Figure 5d. The 800 MHz curve, σ^0_{wM}, has been shifted down by 3 dB for ease of comparison, whilst the cross-polarized curve is normalized to the maximum co-polarized value. It is the fluctuations in dB, not the absolute values, that are important here. Any comparison we make refers to their respective relative changes up-glacier from stake 6 (0 km).

We use the 800 MHz radar profile to identify clear layering in the superimposed ice and firn. At this wavelength the response is less influenced by scattering and more the result of coherent reflections at dielectric interfaces. This is seen by the continuity of interfaces over tens to hundreds of

https://doi.org/10.3189/002214309788608660 Published online by Cambridge University Press

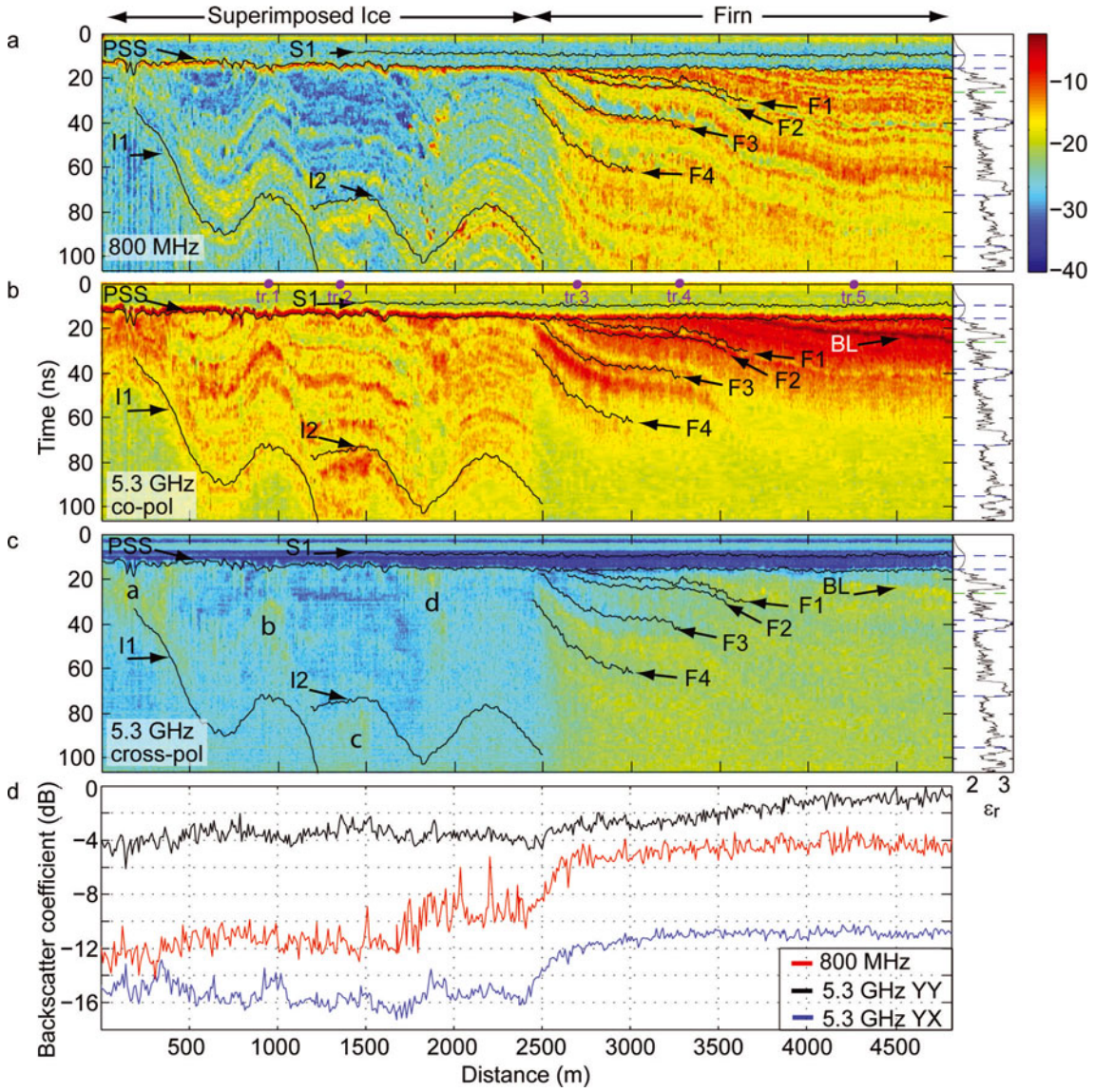

Fig. 5. (a–c) Normalized scattering cross-section, σ_{wq}, at (a) 800 MHz, (b) 5.3 GHz *YY* and (c) 5.3 GHz *YX* (normalized with respect to *YY*). Colour bar shows scale in dB. Horizons digitized on the 800 MHz profile in the snow (S1), previous summer surface (PSS), superimposed ice (I1, I2), and firn (F1–F4) are shown as black curves. At the right end of each radargram, a profile of the average permittivity of the five firn cores is shown with the approximate time location of the digitized horizons at stake 8. The points marked tr.1–5 correspond to the locations of the traces in Figure 7. (d) Normalized backscatter coefficient, σ^0_{wq}, along the profile. The 5.3 GHz cross-polarized response is normalized with respect to the co-polarized response, and the 800 MHz profile has been shifted down by 3 dB for ease of comparison.

metres. Interfaces digitized on the 800 MHz profile are superimposed on the radargrams, giving a reference by which to judge the 5.3 GHz response (Fig. 5).

Radar response to superimposed ice

The superimposed ice area extends up-glacier from 0 to 2.5 km. It has a clearly different radar signature compared to the firn for both frequencies and polarizations shown (Fig. 5a–c). The undulations are caused by variable rates of superimposed ice accumulation influenced by topography, as discussed above. The cause of the layering and reflections is discussed below.

The superimposed ice core revealed that bubbles of the order of 1–5 mm predominate at this location in the superimposed ice, but larger bubbles of the order of 10 mm and smaller bubbles are also seen. Comparison of the processed digital imagery of the superimposed ice core with the radargram (Fig. 6a) indicates that the areas of high bubble content (red) correspond well with the bands of higher backscatter. The exact vertical positioning of the core within the radargram is dependent on the velocity profile used to convert the core depth axis to time and also the positioning of the core with respect to the PSS. To address the former, we show the core with time axes converted using ±10% of our CMP velocity (Fig. 6b and c). The relationship of high bubble content and high backscatter holds well for the lower velocity, but breaks down at depth for the higher velocity. Still, the fit is good enough to suggest that, in the superimposed ice, the reflection horizons in the radar profiles are the result of density contrasts caused by varying bubble content.

The cores and radar data thus show that, using 800 MHz, the greatest reflection occurs at the PSS due to the relatively high permittivity contrast there (snow to ice). Below the PSS, the density contrast between the layers is relatively small, hence the lower backscatter compared to firn (discussed

https://doi.org/10.3189/002214309788608660 Published online by Cambridge University Press

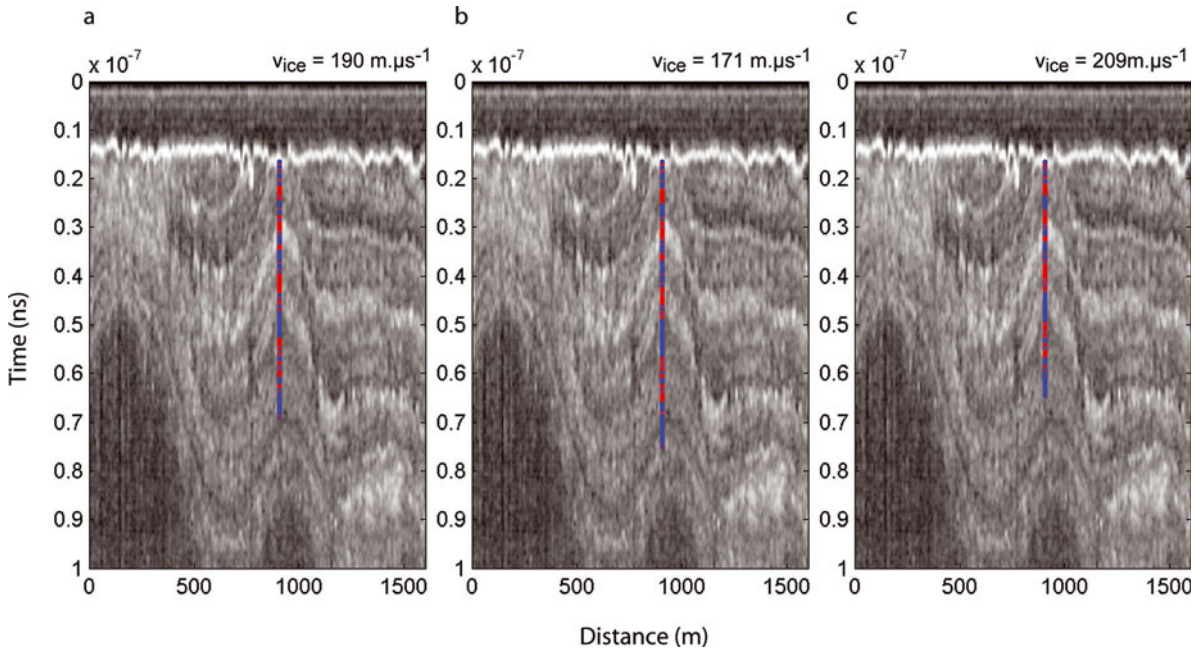

Fig. 6. Comparison of the 5.3 GHz co-polarized radargram with the integrated, normalized, smoothed and thresholded (70%) superimposed ice core. Blue represents low bubble content; red represents high bubble content. Depth-to-time conversion of the core was performed with a velocity of (a) 190 m μs^{-1}, the bulk CMP velocity, (b) 171 m μs^{-1} and (c) 209 m μs^{-1}.

later). The evolution of σ^0_{wM} through the superimposed ice area (Fig. 5d; 0–2.5 km) is a consequence of both the number of layers per metre depth and the overall depth of the superimposed ice. More interfaces over a given depth result in more reflections and thus a higher σ^0_{wM}. An increase in the vertical extent of the superimposed ice leads to an increase in the number of potential reflection horizons, leading to an increase in σ^0_{wM} down to the penetration limit of the radar system (which is at least as great as the time window here).

At 5.3 GHz the PSS induces both a co- and a cross-polarized response (Fig. 7a), and is therefore probably a rough interface. Within the ice below, relatively strong reflections at layer interfaces dominate the co-polarized response, as at 800 MHz, giving the clear layered structure (Fig. 5b). Scattering also occurs at the interfaces and to a lesser extent between them (Fig. 5c). With a wavelength of ~3 cm in ice, the scattering is probably due to the size and distribution of the air-bubble inclusions, which are mostly sub-centimetre size, rather than individual air bubbles. The areas of very low backscatter, i.e. at ~30 ns between 1100 and 1600 m for both the co- and cross-polarized response, are interpreted as ice with very few or very small air bubbles. Such clear layers are less common in the upper 500 m of superimposed ice (2000–2500 m), which has a different structure than the down-glacier superimposed ice (0–2000 m). In this upper 0.5 km of the profile, horizons are less distinct and more closely spaced (more layers per unit depth), resulting in more uniform scattering over depth (Fig. 5b and c). The reason for this difference could be related to the proximity to the firn line.

In the superimposed ice, a number of isolated patches of strong incoherent scattering occur, indicating areas of more complex structure. These are labelled 'a'–'d' in Figure 5c. In cases where the increased scattering is aligned along a horizon, it is attributed to more favourable bubble size/distribution. Patches 'b' and 'c' are of this sort. Patch 'a' lies below a surface drainage channel clearly seen in the PSS. The relic and existing drainage structures could well be the cause of the greater scattering. Patch 'b' also lies beneath an area of higher drainage (assumed from the anticline nature of the layers), and thus may also be associated with this. Patch 'd' is composed of a number of isolated patches, not fully resolved by the 5.3 GHz radar, but clear at 800 MHz (Fig. 5a). The cause of these is unknown, but similar reflections have been observed with an 800 MHz radar on Austfonna, Svalbard (personal communication from T. Dunse, 2007).

Radar response to firn

The firn area extends up-glacier from 2.5 km and is characterized by gently up-glacier-dipping layers. Although visually quite distinct, the transition from superimposed ice to firn is likely to be a zone where the two facies inter-finger somewhat due to fluctuations of the snowline over time. Indeed horizons can be traced across this transition zone (e.g. the layer marked F4 (Fig. 5a)).

Cores taken in the firn area reveal it to be a highly variable medium, with ice lenses varying in thickness from millimetres to >0.5 m over relatively short horizontal distances. The digital images reveal a degree of heterogeneity not apparent in the DEP record (due to the across-core averaging in the latter), with layers sloping at 10–15° and vertical ice fingers, sometimes present on just one side of the core slice (the photographed slices are 7.5 cm wide). We observe that features more than 0.15 m thick are traceable between cores (approximately 10 m), while thinner ice features are highly irregular and localized. We refer to the thicker traceable features as ice layers, and the thinner less extensive features as ice lenses.

Comparison of the cores with the 800 MHz radar profile shows that, below the PSS, reflection horizons correspond to firn–ice interfaces. Phase changes at these interfaces are in agreement with the expected permittivity changes,

https://doi.org/10.3189/002214309788608660 Published online by Cambridge University Press

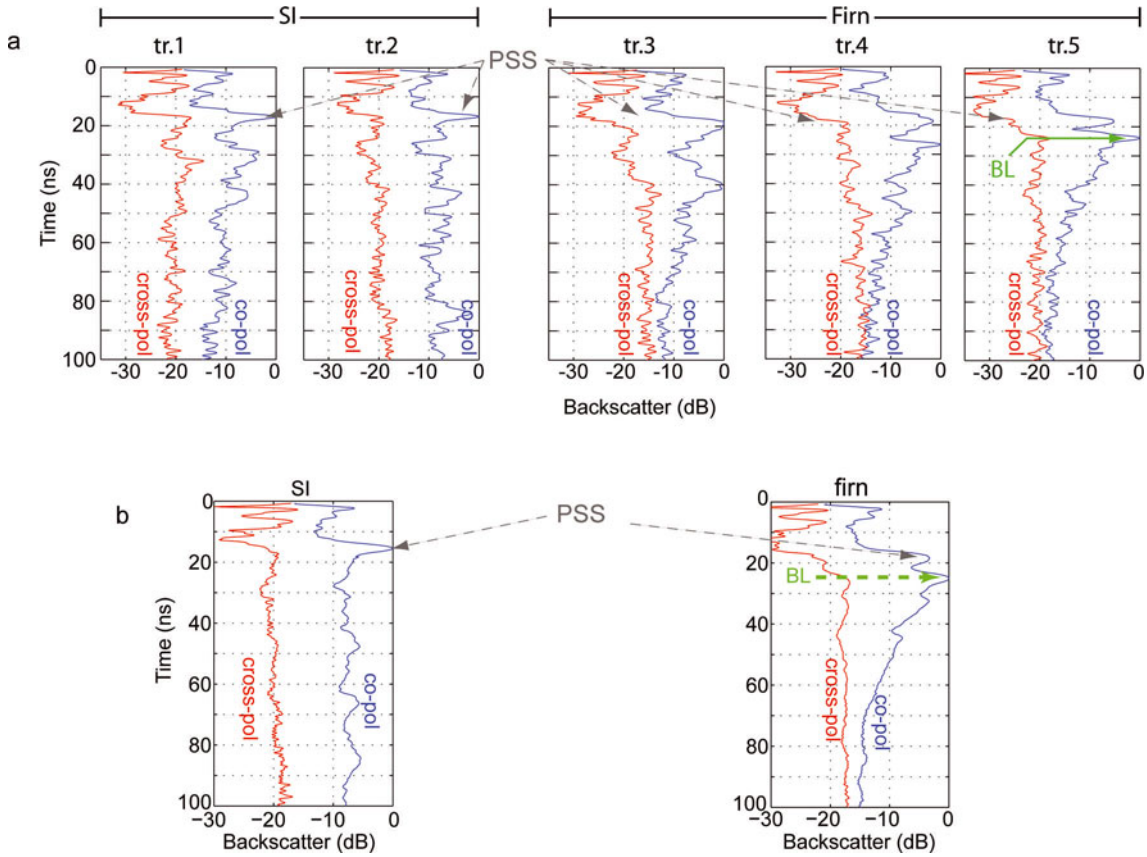

Fig. 7. (a) Traces illustrating the 5.3 GHz co-polarized and cross-polarized normalized scattering cross-section extracted from Figure 5. The cross-polarized response is given in red and the co-polarized response in blue. (b) Co-polarized and cross-polarized backscatter trends over depth for the superimposed ice and firn areas. Each trace is an average of 100 consecutive traces. The PSS response is indicated by the dashed grey arrows. Reflection horizon at the bright layer (BL in Fig. 5 and text) is marked.

i.e. incoming wavelet has the same phase polarity as the emitted wavelet if the reflection is caused at an interface of low to high permittivity, such as firn to ice, and is reversed when the interface goes from high to low permittivity, such as from ice to firn (Fig. 8). To interpret the radargram away from the core sites, we use the phase of the radar reflection to indicate the ordering of firn/ice layering (Arcone and others 1995). Layers F1–F4 are associated with the top and bottom of relatively thick ice layers (Fig. 5a). We find that for thick ice layers, the firn–ice interfaces give more continuous reflection horizons whilst the actual ice body is a low-backscatter band in the radar profile (compare the end of the radar profile in Figure 5a with the averaged DEP profile; low-backscatter layers correspond to ice layers, i.e. high permittivity). Smaller ice lenses that are not so laterally extensive give a more clutter-rich response where individual ice lenses cannot be easily traced. At 800 MHz (wavelength 37.5 cm in air, 26.5 cm in firn of $\varepsilon_r = 2$), scattering from firn grains almost certainly does not occur. Depth-hoar layers may also play a role, but the lower preservation potential of these low-density, coarse layers (common in firn exposed to extensive summertime percolation) makes them hard to capture in the cores.

At 5.3 GHz, scattering is much more effective in the firn than in the superimposed ice. This is seen by the much greater increase in the total relative cross-polarized backscatter compared to co-polarized backscatter (Fig. 5d at ~2500 m). The wave is attenuated, and strong coherent reflections are limited to the upper 50 ns of signal penetration.

Low-backscatter areas are apparent for both co- and cross-polarized responses. These were identified as ice layers in the 800 MHz profile. The traced interfaces indicate that, while there is a coherent response at the top and bottom of the ice layers in the final (down-glacier) 1 km of firn, scattering is not concentrated there (Fig. 5b and c; F1–F4 at 2500–3500 m). Rather, scattering tends to be stronger in the areas between the large ice layers where firn is presumably intermixed with thinner, laterally less extensive ice lenses and pipes, resulting in clutter-rich radar layers at this frequency.

Particularly notable is the bright layer labelled BL in Figure 5b and c, which, for the co-polarized response, is on average 5 dB brighter than the PSS. The narrow width of the reflector and lateral extent suggests that it is associated with a continuous feature. Interestingly, it is approximately at the depth of BL that strong scattering appears to start and continues over depth in the cross-polarized response (Fig. 7b).

Comparison of the location of this reflection with the DEP core profiles places it approximately 1 ns (approximately 11 cm) below the base of the first sizable ice layer (Fig. 9; ice layer at 23–27 ns). This location is in agreement with the depth of BL at the upstream end of the along-glacier profile (Fig. 5b; compare the end of the radargram with the permittivity profile, which is an average of all five DEP profiles). We believe this reflection is associated with the base of the ice layer, but there are uncertainties including: (a) radar resolution (at best 10 cm in ice),

https://doi.org/10.3189/002214309788608660 Published online by Cambridge University Press

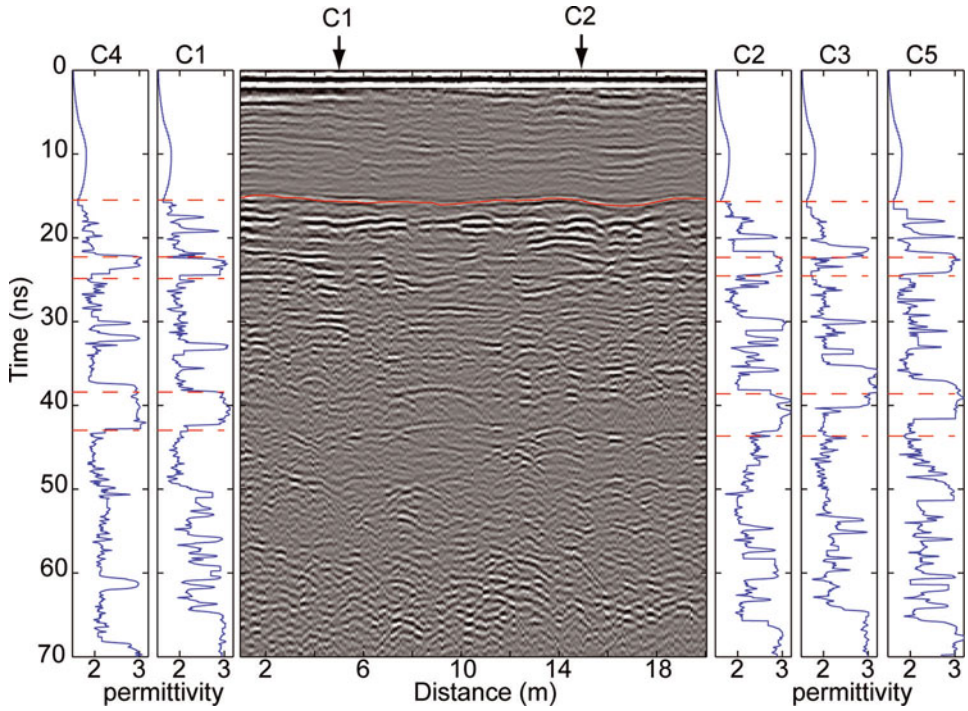

Fig. 8. 800 MHz profile in grid section at stake 8 in the firn area (Fig. 1). The profile passes over cores 1 and 2 at the approximate locations indicated by the arrows. The DEP-derived permittivity profiles for the five cores, C1–C5, are shown either side of the radargram. Red dashed lines show the mean depth (in ns) of the interfaces.

(b) possible delay of response peaks due to scattering, (c) possible digitization uncertainties, and (d) uncertainties in the velocity profile (±10% would result in a 1 cm shift up or down). That the reflection comes from the base of an ice lens as opposed to the top is reasonable. The upper boundary of an ice layer is expected to be more irregular due to feeder ice fingers, or due to differential lateral spreading and freezing of meltwater. This upper boundary may exhibit a more gradual change from firn to ice, giving a less discrete permittivity contrast. In the 800 MHz radargram, the bases of ice lenses are certainly easier to follow than the tops.

Why this ice layer should cause such a strong backscatter response at 5.3 GHz compared to 800 MHz is unclear, but is surely linked to some physical property of the horizon. Close inspection of the firn cores reveals that the first large ice layer (Fig. 4; 23–27 ns) contains a lot of bubble inclusions similar in size and structure to those observed in the superimposed ice core, and thus potential scattering sources at 5.3 GHz. Excavation of the layer may help resolve this question.

Averaging a number of traces (100 traces) in both the superimposed ice and the firn areas gives the backscatter trend over depth (Fig. 7b). Although we cannot identify specific scattering sources from this, it provides insight into the differences between the two areas with respect to the scattering mechanisms. In the superimposed ice area (below the PSS response), the magnitudes of both the co- and the cross-polarized responses remain approximately parallel and constant over depth (Fig. 7b). In the firn area (below the PSS response), the magnitude of the co-polarized response drops off exponentially, whilst that of the cross-polarized response increases very slightly by ~1 dB. This confirms that scattering is significant in the firn where greater depolarization of the wave occurs the greater distance it travels through the medium.

CONCLUSIONS

This paper focuses on a comparison of GPR data at two frequencies, 800 MHz and 5.3 GHz. The purpose is to gain an understanding of the scattering sources in the accumulation area of a glacier relevant to polarimetric 5.3 GHz radars, a frequency commonly used for satellite SAR instruments. Along-glacier profiles are complemented by a shorter, more densely sampled radar grid in the firn area and cores taken within the superimposed ice and firn areas.

The 5.3 GHz response consists of both coherent surface reflections (because of the nadir look angle), shown by the co-polarized response, and incoherent scattering due to rough interfaces and volume scattering, shown by the cross-polarized response.

Based on our observations, we suggest the following mechanisms to explain the scattering cross-section and evolution of the backscatter coefficient at 5.3 GHz. Superimposed ice is a series of ice layers which are distinguished by their variable air-bubble content (related to the conditions under which the superimposed ice formed). Coherent reflections and scattering, caused by the size and distribution of the bubbles, occur both at layer boundaries and within layers. As well as favourable air-bubble size and distribution, drainage structures, both relic and active, cause depolarization of the EM wave and give relatively strong cross-polarized responses. Evolution of the σ^0_{wYY} is linked to the increasing depth of superimposed ice up-glacier. For σ^0_{wYX}, there is a generally low signal level, but the bright patches marked 'a'–'d' in Fig. 5c are clearly visible. At 800 MHz the vertical layering caused by the

https://doi.org/10.3189/002214309788608660 Published online by Cambridge University Press

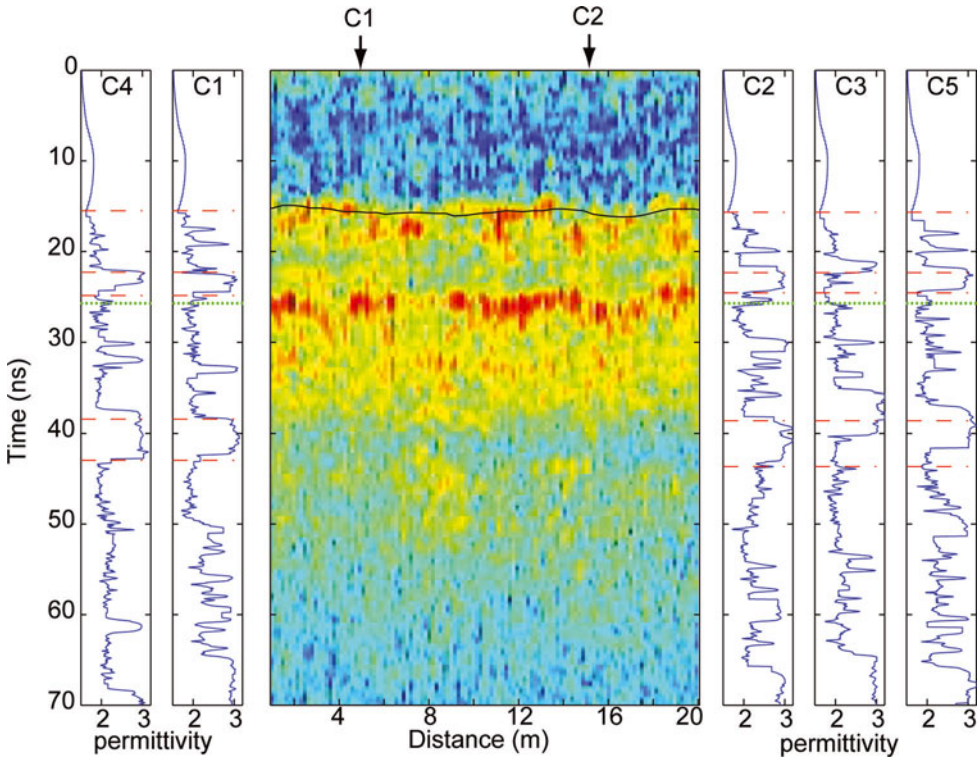

Fig. 9. 5.3 GHz co-polarized profile in the grid at stake 8 in the firn area (Fig. 1). The profile passes over cores C1 and C2. The approximate location of the cores is indicated by the arrows. The DEP-derived permittivity profiles for the five cores, C1–C5, are shown either side of the radargram. Red dashed lines are the mean depth of interfaces digitized on the 800 MHz grid profile. The green dashed line is the mean depth of the bright layer (BL).

density variations related to the air-bubble distribution is also clear.

In the firn, the 5.3 GHz response is dominated by scattering, but with a notable coherent contribution in the first 50 ns. Thicker ice layers, on the order of tens of cm thick, are low-backscatter layers because of their more homogeneous composition. The more heterogeneous firn/ice lens mixture is responsible for significant backscattering for both co- and cross-polarized responses. We do not rule out the possibility of depth hoar, and bubbles within the thicker ice layers also contributing through volume scattering. At 800 MHz, interface reflections are easier to trace and are visible to a greater depth because there is less scattering. Laterally extensive, high-backscatter interfaces do occur at 5.3 GHz and are probably associated with the base of thicker ice layers, or facies just below, possibly depth-hoar layers. The coherent component is not so important for side-looking satellite instruments, but the strong incoherent scattering that occurs would be of significance.

ACKNOWLEDGEMENTS

We thank R. Storvold and K.-A. Høgda of the Northern Research Institute Tromsø (Norut, Tromsø) for drilling the superimposed ice core and discussions on scattering. J.O. Hagen of the University of Oslo, and J. Kohler of the Norwegian Polar Institute provided support in the field and fruitful discussions concerning the data. C. Nuth is thanked for helping to process the cores. This work was supported in part by the Norwegian Research Council (NRF) under contract 155834 and in part by the Norwegian Polar Institute under an Arctic research grant. The paper was greatly improved thanks to thoughtful reviews.

REFERENCES

Arcone, S.A. 2002. Airborne-radar stratigraphy and electrical structure of temperate firn: Bagley Ice Field, Alaska, USA. *J. Glaciol.*, **48**(161), 317–334.

Arcone, S.A., D.E. Lawson and A.J. Delaney. 1995. Short-pulse radar wavelet recovery and resolution of dielectric contrasts within englacial and basal ice of Matanuska Glacier, Alaska, U.S.A. *J. Glaciol.*, **41**(137), 68–86.

Bamber, J.L. and R. Kwok. 2004. Remote sensing techniques. *In* Bamber, J.L. and A.J. Payne, *eds. Mass balance of the cryosphere: observations and modelling of contemporary and future changes.* Cambridge, Cambridge University Press, 59–113.

Berthier, E., Y. Arnaud, C. Vincent and F. Rémy. 2006. Biases of SRTM in high-mountain areas: implications for the monitoring of glacier volume changes. *Geophys. Res. Lett.*, **33**(8), L08502. (10.1029/2006GL025862.)

Bjørnsson, H. *and 6 others.* 1996. The thermal regime of sub-polar glaciers mapped by multi-frequency radio-echo sounding. *J. Glaciol.*, **42**(140), 23–32.

Bøggild, C.E., R. Forsberg and N. Reeh. 2005. Meltwater retention in a transect across the Greenland ice sheet. *Ann. Glaciol.*, **40**, 169–173.

Brandt, O., J. Kohler and M. Lüthje. 2008. Spatial mapping of multi-year superimposed ice on the glacier Kongsvegen, Svalbard. *J. Glaciol.*, **54**(184), 73–80.

Daniels, D.J. 2004. *Ground penetrating radar. Second edition.* London, Institution of Electrical Engineers.

Eisen, O., U. Nixdorf, F. Wilhelms and H. Miller. 2002. Electromagnetic wave speed in polar ice: validation of the common-midpoint technique with high-resolution dielectric-profiling and γ-density measurements. *Ann. Glaciol.*, **34**, 150–156.

Hamran, S.-E. and K. Langley. 2006. C-band polarimetric GPR. *In* Daniels, J.J. and C.-C. Chen, *eds. GPR 2006: Proceedings of the 11th International Conference on Ground Penetrating Radar, 19–22 June 2006, Columbus OH.* CD-ROM.

https://doi.org/10.3189/002214309788608660 Published online by Cambridge University Press

Hawley, R.L., E.M. Morris, R. Cullen, U. Nixdorf, A.P. Shepherd and D.J. Wingham. 2006. ASIRAS airborne radar resolves internal annual layers in the dry-snow zone of Greenland. *Geophys. Res. Lett.,* **33**(4), L04502. (10.1029/2005GL025147.)

Helm, V. *and 6 others*. 2007. Winter accumulation in the percolation zone of Greenland measured by airborne radar altimeter. *Geophys. Res. Lett.,* **34**(6), L06501. (10.1029/2006GL029185.)

Jezek, K.C., P. Gogineni and M. Shanableh. 1994. Radar measurements of melt zones on the Greenland ice sheet. *Geophys. Res. Lett.,* **21**(1), 33–36.

Kohler, J., J.C. Moore and E. Isaksson. 2003. Comparison of modelled and observed responses of a glacier snowpack to ground-penetrating radar. *Ann. Glaciol.,* **37**, 293–297.

König, M., J. Wadham, J.G. Winther, J. Kohler and A.-M. Nuttall. 2002. Detection of superimposed ice on the glaciers Kongsvegen and midre Lovénbreen, Svalbard, using SAR satellite imagery. *Ann. Glaciol.,* **34**, 335–342.

Kovacs, A., A.J. Gow and R.M. Morey. 1995. The in-situ dielectric constant of polar firn revisited. *Cold Reg. Sci. Technol.,* **23**(3), 245–256.

Lacroix, P., B. Legrésy, R. Coleman, M. Dechambre and F. Rémy. 2007. Dual-frequency altimeter signal from Envisat on the Amery ice-shelf. *Remote Sens. Environ.,* **109**(3), 285–294.

Langley, K. *and 6 others*. 2007. Use of C-band ground penetrating radar to determine backscatter sources within glaciers. *IEEE Trans. Geosci. Remote Sens.,* **45**(5), 1236–1246.

Legrésy, B., F. Papa, F. Rémy, G. Vinay, M. van den Bosch and O.-Z. Zanife. 2005. ENVISAT radar altimeter measurements over continental surfaces and ice caps using the ICE-2 retracking algorithm. *Remote Sens. Environ.,* **95**(2), 150–163.

Liestøl, O. 1988. The glaciers in the Kongsfjorden area, Spitsbergen. *Nor. Geogr. Tidsskr.,* **42**(4), 231–238.

Melvold, K. and J.O. Hagen. 1998. Evolution of a surge-type glacier in its quiescent phase: Kongsvegen, Spitsbergen, 1964–95. *J. Glaciol.,* **44**(147), 394–404.

Obleitner, F. and M. Lehning. 2004. Measurement and simulation of snow and superimposed ice at the Kongsvegen glacier, Svalbard (Spitzbergen). *J. Geophys. Res.,* **109**(D4), D04106. (10.1029/2003JD003945.)

Paterson, W.S.B. 1994. *The physics of glaciers. Third edition.* Oxford, etc., Elsevier.

Rignot, E., K. Echelmeyer and W. Krabill. 2001. Penetration depth of interferometric synthetic-aperture radar signals in snow and ice. *Geophys. Res. Lett.,* **28**(18), 3501–3504.

Robin, G.de Q., S. Evans and J.T. Bailey. 1969. Interpretation of radio echo sounding in polar ice sheets. *Philos. Trans. R. Soc. London, Ser. A,* **265**(1166), 437–505.

Sarabandi, K., F.T. Ulaby and M.A. Tassoudji. 1990. Calibration of polarimetric radar systems with good polarization isolation. *IEEE Trans. Geosci. Remote Sens.,* **28**(1), 70–75.

Scott, J., D. Mair, P. Nienow, V. Parry and E. Morris. 2006a. A ground-based radar backscatter investigation in the percolation zone of the Greenland Ice Sheet. *Remote Sens. Environ.,* **104**(4), 361–373.

Scott, J., P. Nienow, V. Parry, D. Mair, E. Morris and D. Wingham. 2006b. The importance of seasonal and annual layers in controlling backscattter to radar altimeters across the percolation zone of an ice sheet. *Geophys. Res. Lett.,* **33**(24), L24502. (10.1029/2006GL027974.)

Sjögren, B. *and 6 others*. 2007. Determination of firn density in ice cores using image analysis. *J. Glaciol.,* **53**(182), 413–419.

Stebler, O., A. Schwerzmann, A. Lüthi, E. Meier and D.R. Nuesch. 2005. Pol-InSAR observations from an Alpine glacier in the cold infiltration zone at L- and P-band. *IEEE Geosci. Remote Sens. Lett.,* **2**(3), 357–361.

Ulaby, F.T., R.K. Moore and A.K. Fung. 1981. *Microwave remote sensing, active and passive. Vol. 1. Fundamentals and radiometry.* Reading, MA, Addison-Wesley Publishing Co.

Wadham, J.L. and A.-M. Nuttall. 2002. Multiphase formation of superimposed ice during a mass-balance year at a maritime high-Arctic glacier. *J. Glaciol.,* **48**(163), 545–551.

Wadham, J., J. Kohler, A. Hubbard, A.-M. Nuttall and D. Rippin. 2006. Superimposed ice regime of a high Arctic glacier inferred using ground-penetrating radar, flow modeling, and ice cores. *J. Geophys. Res.,* **111**(F1), F01007. (10.1029/2004JF000144.)

Wilhelms, F., J. Kipfstuhl, H. Miller, K. Heinloth and J. Firestone. 1998. Precise dielectric profiling of ice cores: a new device with improved guarding and its theory. *J. Glaciol.,* **44**(146), 171–174

MS received 2 July 2007 and accepted in revised form 3 October 2008

https://doi.org/10.3189/002214309788608660 Published online by Cambridge University Press